

# Secular Dynamics of an Exterior Test Particle: The Inverse Kozai and Other Eccentricity-Inclination Resonances

Benjamin R. Vinson<sup>1★</sup>, Eugene Chiang<sup>2,3†</sup>

<sup>1</sup>*Department of Physics, 366 LeConte Hall, University of California, Berkeley, 94720, USA*

<sup>2</sup>*Department of Astronomy, 501 Campbell Hall, University of California, Berkeley 94720-3411, USA*

<sup>3</sup>*Department of Earth and Planetary Science, 307 McCone Hall, University of California, Berkeley 94720, USA*

20 August 2021

## ABSTRACT

The behavior of an interior test particle in the secular three-body problem has been studied extensively. A well-known feature is the Lidov-Kozai resonance in which the test particle’s argument of periastron librates about  $\pm 90^\circ$  and large oscillations in eccentricity and inclination are possible. Less explored is the inverse problem: the dynamics of an exterior test particle and an interior perturber. We survey numerically the inverse secular problem, expanding the potential to hexadecapolar order and correcting an error in the published expansion. Four secular resonances are uncovered that persist in full  $N$ -body treatments (in what follows,  $\varpi$  and  $\Omega$  are the longitudes of periastron and of ascending node,  $\omega$  is the argument of periastron, and subscripts 1 and 2 refer to the inner perturber and the outer test particle): (i) an orbit-flipping quadrupole resonance requiring a non-zero perturber eccentricity  $e_1$ , in which  $\Omega_2 - \varpi_1$  librates about  $\pm 90^\circ$ ; (ii) a hexadecapolar resonance (the “inverse Kozai” resonance) for perturbers that are circular or nearly so and inclined by  $I \simeq 63^\circ/117^\circ$ , in which  $\omega_2$  librates about  $\pm 90^\circ$  and which can vary the particle eccentricity by  $\Delta e_2 \simeq 0.2$  and lead to orbit crossing; (iii) an octopole “apse-aligned” resonance at  $I \simeq 46^\circ/107^\circ$  wherein  $\varpi_2 - \varpi_1$  librates about  $0^\circ$  and  $\Delta e_2$  grows with  $e_1$ ; and (iv) an octopole resonance at  $I \simeq 73^\circ/134^\circ$  wherein  $\varpi_2 + \varpi_1 - 2\Omega_2$  librates about  $0^\circ$  and  $\Delta e_2$  can be as large as 0.3 for small but non-zero  $e_1$ . Qualitatively, the more eccentric the perturber, the more the particle’s eccentricity and inclination vary; also, more polar orbits are more chaotic. Our solutions to the inverse problem have potential application to the Kuiper belt and debris disks, circumbinary planets, and hierarchical stellar systems.

**Key words:** celestial mechanics – binaries: general – planets and satellites: dynamical evolution and stability – Kuiper belt: general

## 1 INTRODUCTION

In the restricted three-body problem, the Lidov-Kozai resonance provides a way for an external perturber to torque test particle orbits to high eccentricity and inclination (Lidov 1962; Kozai 1962). When the perturber’s orbit is circular ( $e_2 = 0$ ), and when the inclination  $I$  between the test particle’s orbit and the perturber’s exceeds  $\arccos \sqrt{3/5} \simeq 39^\circ$ , the test particle’s argument of periastron  $\omega_1$  can librate (oscillate) about either  $90^\circ$  or  $270^\circ$ : these are the fixed points of the Lidov-Kozai (“Kozai” for short) resonance.<sup>1</sup> The larger

the libration amplitude, the greater the eccentricity variations. For circular perturbers, the test particle eccentricity  $e_1$  can cycle between 0 and 1 as the inclination  $I$  cycles between  $90^\circ$  and  $39^\circ$ ;<sup>2</sup>  $e_1$  and  $I$  seesaw to conserve  $J_{1z} \propto \sqrt{1 - e_1^2} \cos I$ , the test particle’s vector angular momentum projected onto the perturber’s orbit normal. For eccentric external perturbers ( $e_2 \neq 0$ ), the gravitational potential is no longer

orbital semimajor axes  $a_1 < a_2$ . These subscripts apply regardless of whether the body is a test particle or a perturber.

<sup>2</sup> There is also a retrograde branch for the standard Kozai resonance in which  $I$  cycles between  $90^\circ$  and  $141^\circ$ . In this paper we will encounter several resonances for which retrograde fixed points are paired with prograde fixed points, but will sometimes focus on the prograde branches for simplicity.

★ E-mail: ben\_vinson@berkeley.edu

† E-mail: echiang@astro.berkeley.edu

<sup>1</sup> Throughout this paper, subscript “1” denotes the interior body and subscript “2” denotes the exterior body; by definition, the

axisymmetric, and the test particle’s  $J_{1z}$  is now free to vary, which it can do with a vengeance: the test particle can start from a nearly coplanar, prograde orbit ( $J_{1z} > 0$ ) and “flip” to being retrograde ( $J_{1z} < 0$ ; e.g., [Lithwick & Naoz 2011](#) and [Katz et al. 2011](#)). The large eccentricities and inclinations accessed by the Kozai mechanism have found application in numerous settings: enabling Jupiter to send comets onto sun-grazing trajectories (e.g., [Bailey et al. 1992](#)); delineating regions of orbital stability for planetary satellites perturbed by exterior satellites and the Sun (e.g., [Carruba 2002](#); [Nesvorny et al. 2003](#); [Tremaine & Yavetz 2014](#)); merging compact object binaries in triple systems (e.g., [Kushnir et al. 2013](#); [Silsbee & Tremaine 2017](#)); and explaining the orbits of eccentric or short-period extrasolar planets (e.g., [Wu & Murray 2003](#)), including warm Jupiters ([Dawson & Chiang 2014](#)), and hot Jupiters with their large spin-orbit obliquities ([Naoz et al. 2011](#)). See [Naoz \(2016\)](#) for a review.

The Kozai resonance is a secular effect (i.e., it does not depend on orbital longitudes, which are time-averaged away from the equations of motion) that applies to an interior test particle perturbed by an exterior body. Curiously, the “inverse” secular problem—an exterior test particle and an interior perturber—does not seem to have received as much attention as the conventional problem. [Gallardo et al. \(2012\)](#) studied the inverse problem in the context of Kuiper belt objects perturbed by Neptune and the other giant planets, idealizing the latter as occupying circular ( $e_1 = 0$ ) and coplanar orbits, and expanding the disturbing function (perturbation potential) to hexadecapolar order in  $\alpha \equiv a_1/a_2$ . They discovered an analogous Kozai resonance in which  $\omega_2$  librates about either  $+90^\circ$  or  $-90^\circ$ , when  $I \simeq \arccos \sqrt{1/5} \simeq 63^\circ$  (see also [Tremaine & Yavetz 2014](#)). Eccentricity variations are stronger inside this “inverse Kozai” or  $\omega_2$  resonance than outside. [Thomas & Morbidelli \(1996\)](#) also assumed the solar system giant planets to be on circular coplanar orbits, dispensing with a multipole expansion and numerically computing secular Hamiltonian level curves for an exterior test particle. For  $a_2 = 45$  AU, just outside Neptune’s orbit, resonances appear at high  $I$  and  $e_2$  that are centered on  $\omega_2 = 0^\circ$  and  $180^\circ$ .

[Naoz et al. \(2017\)](#) also studied the inverse problem, expanding the potential to octopolar order and considering non-zero  $e_1$ . Orbit flipping was found to be possible via a quadrupole-level resonance that exists only when  $e_1 \neq 0$  and for which  $\Omega_2 - \varpi_1$  librates about either  $+90^\circ$  or  $-90^\circ$ . Here  $\Omega$  and  $\varpi$  are the longitudes of ascending node and of periastron, respectively. As  $e_1$  increases, the minimum  $I$  at which orbits can flip decreases. All of this inclination behavior obtains at the quadrupole level; the  $\Omega_2 - \varpi_1$  resonance was also uncovered by [Verrier & Evans \(2009\)](#) and studied analytically by [Farago & Laskar \(2010\)](#). Octopole terms were shown by [Naoz et al. \(2017\)](#) to enable test particles to alternate between one libration center ( $\Omega_2 - \varpi_1 = +90^\circ$ ) and another ( $\Omega_2 - \varpi_1 = -90^\circ$ ), modulating the inclination evolution and introducing chaos, particularly at high  $e_1$ .

In this paper we explore more systematically the inverse problem, expanding the perturbation potential to hexadecapolar order and considering non-zero  $e_1$ . In addition to studying more closely the hexadecapolar inverse Kozai resonance found by [Gallardo et al. \(2012\)](#) and how it alters when  $e_1$  increases, we will uncover strong, octopolar resonances

not identified by [Naoz et al. \(2017\)](#). By comparison with the latter work, we focus more on the test particle’s eccentricity variations than on its inclination variations. We are interested, for example, in identifying dynamical channels that can connect planetary systems with more distant reservoirs of minor bodies, e.g., the “extended scattered” or “detached” Kuiper belt (e.g., [Sheppard & Trujillo 2016](#)), or the Oort cloud (e.g., [Silsbee & Tremaine 2016](#)). Another application is to extrasolar debris disks, some of whose scattered light morphologies appear sculpted by eccentric perturbers (e.g., [Lee & Chiang 2016](#)). We seek to extend such models to large mutual inclinations (e.g., [Verrier & Evans 2008](#); [Pearce & Wyatt 2014](#); [Nesvold et al. 2016](#); [Zanardi et al. 2017](#)).

This paper is organized as follows. In Section 2 we write down the secular disturbing function of an interior perturber to hexadecapolar order in  $\alpha = a_1/a_2$ . There we also fix certain parameters (masses and semimajor axes; e.g.,  $\alpha = 0.2$ ) for our subsequent numerical survey. Results for a circular perturber are given in Section 3 and for an eccentric perturber in Section 4, with representative secular integrations tested against  $N$ -body integrations. We wrap up in Section 5.

## 2 SECULAR DISTURBING FUNCTION FOR EXTERIOR TEST PARTICLE

The disturbing function of [Yokoyama et al. \(2003](#), hereafter Y03) is for the conventional problem: an interior test particle (satellite of Jupiter) perturbed by an exterior body (the Sun). We may adapt their  $R$  to our inverse problem of an exterior test particle perturbed by an interior body by a suitable reassignment of variables. This reassignment is straightforward because the disturbing function is proportional to  $1/\Delta$ , where  $\Delta$  is the absolute magnitude of the distance between the test particle and the perturber (Y03’s equation 2, with the indirect term omitted because that term vanishes after secular averaging). This distance  $\Delta$  is obviously the same between the conventional and inverse problems, and so the Legendre polynomial expansion of  $1/\Delta$  performed by Y03 for their problem holds just as well for ours.

The change of variables begins with a simple replacing of subscripts. We replace Y03’s subscript  $\odot$  (representing the Sun, their exterior perturber) with “2” (our exterior test particle). For their unsubscripted variables (describing their interior test particle), we add a subscript “1” (for our interior perturber). Thus we have:

$$a \rightarrow a_1 \tag{1}$$

$$a_\odot \rightarrow a_2 \tag{2}$$

$$e \rightarrow e_1 \tag{3}$$

$$e_\odot \rightarrow e_2, \tag{4}$$

where  $a$  is the semimajor axis and  $e$  is the eccentricity. Since we are interested in the inverse problem of an interior perturber, we replace their perturber mass  $M_\odot$  with our perturber mass:

$$M_\odot \rightarrow m_1. \tag{5}$$

Their inclination  $I$  is the mutual inclination between the interior and exterior orbits; we leave it as is.

Mapping of the remaining angular variables requires more care. Y03's equations (6) and (7) take the reference plane to coincide with the orbit of the exterior body—this is the invariable plane when the interior body is a test particle. We want the reference plane to coincide instead with the orbit of the interior body (the invariable plane for our inverse problem). To convert to the new reference plane, we use the relation

$$\Omega_1 - \Omega_2 = \pi \quad (6)$$

for longitude of ascending node  $\Omega$ , valid whenever the reference plane is the invariable plane for arbitrary masses 1 and 2 (the vector pole of the invariable plane is co-planar with the orbit normals of bodies 1 and 2, and lies between them). We therefore map Y03's  $\Omega$  to

$$\Omega \rightarrow \Omega_1 \rightarrow \Omega_2 + \pi, \quad (7)$$

and their argument of periastron  $\omega$  to

$$\omega \equiv (\varpi - \Omega) \rightarrow (\varpi_1 - \Omega_1) \rightarrow (\varpi_1 - \pi - \Omega_2) \quad (8)$$

where  $\varpi$  is the longitude of periastron. Although  $\varpi_1$  remains meaningful in our new reference plane,  $\Omega_1$  and  $\omega_1$  are no longer meaningful, and are swapped out using (7) and (8). Finally

$$\varpi_\odot \rightarrow \varpi_2. \quad (9)$$

Armed with (1)–(9), we re-write equations (6)–(8) of Y03 to establish the secular disturbing function  $R$  for an exterior test particle perturbed by an interior body of mass

$m_1$ , expanded to hexadecapole order:

$$b_1 = -(5/2)e_1 - (15/8)e_1^3 \quad (10)$$

$$b_2 = -(35/8)e_1^3 \quad (11)$$

$$c_1 = Gm_1 a_1^2 \frac{1}{a_2^3 (1 - e_2^2)^{3/2}} \quad (12)$$

$$c_2 = Gm_1 a_1^3 \frac{e_2}{a_2^4 (1 - e_2^2)^{5/2}} \quad (13)$$

$$c_3 = Gm_1 a_1^4 \frac{1}{a_2^5 (1 - e_2^2)^{7/2}} \quad (14)$$

$$d_1^* = 1 + (15/8)e_1^2 + (45/64)e_1^4 \quad (15)$$

$$d_2 = (21/8)e_1^2(2 + e_1^2) \quad (16)$$

$$d_3 = (63/8)e_1^4 \quad (17)$$

$$cI \equiv \cos I \quad (18)$$

$$sI \equiv \sin I \quad (19)$$

$$R_2 = \frac{1}{8} \left( 1 + \frac{3}{2}e_1^2 \right) (3cI^2 - 1) + \frac{15}{16}e_1^2 sI^2 \cos 2(\Omega_2 - \varpi_1) \quad (20)$$

$$\begin{aligned} R_3 = \frac{1}{64} & \left[ (-3 + 33cI + 15cI^2 - 45cI^3) b_1 \cos(\varpi_2 + \varpi_1 - 2\Omega_2) \right. \\ & + (-3 - 33cI + 15cI^2 + 45cI^3) b_1 \cos(\varpi_2 - \varpi_1) \\ & + (15 - 15cI - 15cI^2 + 15cI^3) b_2 \cos(\varpi_2 + 3\varpi_1 - 4\Omega_2) \\ & \left. + (15 + 15cI - 15cI^2 - 15cI^3) b_2 \cos(\varpi_2 - 3\varpi_1 + 2\Omega_2) \right] \quad (21) \end{aligned}$$

$$\begin{aligned} R_4 = \frac{3}{16} & \left( 2 + 3e_2^2 \right) d_1^* - \frac{495}{1024}e_2^2 - \frac{135}{256}cI^2 - \frac{165}{512} \\ & + \frac{315}{512}cI^4 + \frac{945}{1024}cI^4 e_2^2 - \frac{405}{512}cI^2 e_2^2 \\ & + \left( \frac{105}{512}cI^4 + \frac{315}{1024}e_2^2 - \frac{105}{256}cI^2 + \frac{105}{512} - \frac{315}{512}cI^2 e_2^2 \right. \\ & \left. + \frac{315}{1024}cI^4 e_2^2 \right) d_3 \cos 4(\varpi_1 - \Omega_2) \\ & + \frac{105}{512} \left( cI^3 - cI - \frac{1}{2}cI^4 + \frac{1}{2} \right) d_3 e_2^2 \cos(4\varpi_1 + 2\varpi_2 - 6\Omega_2) \\ & + \frac{105}{512} \left( -cI^3 + cI - \frac{1}{2}cI^4 + \frac{1}{2} \right) d_3 e_2^2 \cos(4\varpi_1 - 2\varpi_2 - 2\Omega_2) \\ & + \left( \frac{45}{64}cI^2 - \frac{45}{512} - \frac{315}{512}cI^4 \right) e_2^2 \cos(2\varpi_2 - 2\Omega_2) \\ & + \left( \frac{15}{16}cI^2 + \frac{45}{32}cI^2 e_2^2 - \frac{45}{256}e_2^2 - \frac{15}{128} - \frac{315}{256}cI^4 e_2^2 \right. \\ & \left. - \frac{105}{128}cI^4 \right) d_2 \cos(2\varpi_1 - 2\Omega_2) \\ & + \left( \frac{15}{256} - \frac{45}{128}cI^2 + \frac{75}{256}cI + \frac{105}{256}cI^4 \right. \\ & \left. - \frac{105}{256}cI^3 \right) d_2 e_2^2 \cos(2\varpi_1 + 2\varpi_2 - 4\Omega_2) \\ & + \left( \frac{15}{256} - \frac{45}{128}cI^2 - \frac{75}{256}cI + \frac{105}{256}cI^4 \right. \\ & \left. + \frac{105}{256}cI^3 \right) d_2 e_2^2 \cos(2\varpi_1 - 2\varpi_2) \quad (22) \end{aligned}$$

$$R = R_2 c_1 + R_3 c_2 + R_4 c_3. \quad (23)$$

A few notes: (i) this disturbing function includes only the

quadrupole ( $R_2c_1$ ), octopole ( $R_3c_2$ ), and hexadecapole ( $R_4c_3$ ) terms; the monopole term has been dropped (it is equivalent to adding  $m_1$  to the central mass  $m_0$ ), as has the dipole term which orbit-averages to zero; (ii) there are typos in equation (6) of Y03: their  $c_i$ 's are missing factors of  $M_\odot$  ( $\rightarrow m_1$ ); (iii) we have starred  $d_1^*$  in equation (15) to highlight that this term as printed in Y03 is in error, as brought to our attention by Matija Čuk, who also provided the correction. We have verified this correction independently by computing the hexadecapole disturbing function in the limit  $I = 0$  and  $e_2 = 0$ .

We insert the disturbing function  $R$  into Lagrange's planetary equations for  $\dot{e}_2$ ,  $\dot{\Omega}_2$ ,  $\dot{\varpi}_2$ , and  $\dot{I}$  (equations 6.146, 6.148, 6.149, and 6.150 of Murray & Dermott 2000). These coupled ordinary differential equations are solved numerically using a Runge-Kutta-Dormand-Prince method with stepsize control and dense output (`runge_kutta_dopri5` in C++).

### 2.1 Fixed Parameters

The number of parameters is daunting, even for the restricted, secular three-body problem considered here. Throughout this paper, we fix the following parameters:

$$a_1 = 20 \text{ AU} \quad (24)$$

$$a_2 = 100 \text{ AU} \quad (25)$$

$$m_0 = 1 M_\odot \quad (26)$$

$$m_1 = 0.001 m_0. \quad (27)$$

The ratio of orbital semimajor axes is fixed at  $\alpha \equiv a_1/a_2 = 0.2$ , the largest value we thought might still be amenable to a truncated expansion in  $\alpha$  of the disturbing function (the smaller is  $\alpha$ , the better the agreement with  $N$ -body integrations, as we have verified explicitly; see also Section 4.3). Many of our results—the existences of secular resonances, and the amplitudes of eccentricity and inclination variations—fortunately do not depend critically on  $\alpha$ ; for a different  $\alpha$ , we can obtain the same qualitative results by adjusting initial eccentricities (see, e.g., Section 3). The above parameter choices do directly determine the timescales of the test particle's evolution, which should (and mostly do) fall within the Gyr ages of actual planetary systems (see Section 3.1.1). Our parameters are those of a distant Jupiter-mass planet (like 51 Eri b; Macintosh et al. 2015) perturbing an exterior collection of minor bodies (like the Kuiper belt).

With no loss of generality, we align the apsidal line of the perturber's orbit with the  $x$ -axis:

$$\varpi_1 = 0^\circ. \quad (28)$$

The remaining variables of the problem are  $e_1$ ,  $e_2$ ,  $I$ ,  $\omega_2$ , and  $\Omega_2$ . Often in lieu of  $e_2$  we will plot the periastron distance  $q_2 = a_2(1 - e_2)$  to see how close the test particle comes to the perturber. Once the orbits cross or nearly cross (i.e., once  $q_2 \lesssim a_1(1 + e_1) = 20\text{--}35 \text{ AU}$ ), our secular equations break down and the subsequent evolution cannot be trusted. Nevertheless we will sometimes show orbit-crossing trajectories just to demonstrate that channels exist whereby test particle periastra can be lowered from large distances to near the perturber (if not conversely).

To the extent that  $R$  is dominated by the first quadrupole term in (20) proportional to  $(3 \cos^2 I - 1)$ , more

positive  $R$  corresponds to more co-planar orbits (i.e., wires 1 and 2 closer together). The numerical values for  $R$  quoted below have been scaled to avoid large unwieldy numbers; they should be multiplied by  $3.55 \times 10^6$  to bring them into cgs units.

### 3 CIRCULAR PERTURBER

When  $e_1 = 0$ , the octopole contribution to the potential vanishes, but the quadrupole and hexadecapole contributions do not.

Because the potential for a circular perturber is axisymmetric, the  $z$ -component of the test particle's angular momentum is conserved (we omit the subscript 2 on  $J_z$  for convenience):

$$J_z \equiv \sqrt{1 - e_2^2} \cos I \quad (29)$$

where we have dropped the dependence of the angular momentum on  $a_2$ , since semimajor axes never change in secular dynamics. We therefore have two constants of the motion:  $J_z$  and the disturbing function itself (read: Hamiltonian),  $R$ . Smaller  $J_z$  corresponds to more highly inclined and/or more eccentric test particle orbits.

#### 3.1 The Inverse Kozai ( $\omega_2$ ) Resonance

Figure 1 gives a quick survey of the test particle dynamics for  $e_1 = 0$ . For a restricted range in  $J_z \approx 0.40\text{--}0.45$ , the test particle's argument of periastron  $\omega_2$  librates about either  $90^\circ$  or  $270^\circ$ , with concomitant oscillations in  $q_2$  (equivalently  $e_2$ ) and  $I$ . This is the analogue of the conventional Kozai resonance, exhibited here by an exterior test particle; we refer to it as the ‘‘inverse Kozai’’ resonance or the  $\omega_2$  resonance. The inverse Kozai resonance appears only at hexadecapole order; it originates from the term in (22) proportional to  $e_2^2 \cos(2\varpi_2 - 2\Omega_2) = e_2^2 \cos 2\omega_2$ .<sup>3</sup>

The inverse Kozai resonance appears near

$$I(\omega_2\text{-res}) = \arccos(\pm\sqrt{1/5}) \approx 63^\circ \text{ and } 117^\circ \quad (30)$$

which, by Lagrange's planetary equations and (20), are the special inclinations at which the quadrupole precession rate

$$\left. \frac{d\omega_2}{dt} \right|_{\text{quad}, e_1=0} = \frac{3}{8} \frac{m_1}{m_0} \left( \frac{a_1}{a_2} \right)^2 \frac{n_2}{(1 - e_2)^2} (5 \cos^2 I - 1) \quad (31)$$

vanishes, where  $n_2$  is the test particle mean motion; see Gallardo et al. (2012, their equation 11 and subsequent discussion). At  $I = I(\omega_2\text{-res})$ , fixed points appear at  $\omega_2 = 90^\circ$  and  $\omega_2 = 270^\circ$ . The critical angles  $63^\circ$  and  $117^\circ$  are related to their well-known Kozai counterparts of  $39^\circ$  and  $141^\circ$  (i.e.,  $\arccos(\pm\sqrt{3/5})$ ), but the correspondence is not exact. In the conventional problem, the inclinations at which the fixed points ( $\omega_1 = \pm 90^\circ$ ,  $\dot{\omega}_1 = 0$ ) appear vary from case

<sup>3</sup> Naoz et al. (2017) refer to their octopole-level treatment as exploring the ‘‘eccentric Kozai-Lidov mechanism for an outer test particle.’’ Our terminology here differs; we consider the analogue of the Kozai-Lidov resonance the  $\omega_2$  resonance, which appears only at hexadecapole order, not the  $\Omega_2 - \varpi_1$  resonance that they highlight.

to case; they are given by  $I = \arccos \left[ \pm \sqrt{(3/5)(1 - e_1^2)} \right] = \arccos \left[ \pm (3/5)^{1/4} |J_{1z}|^{1/2} \right]$ , where  $J_{1z} \equiv \sqrt{1 - e_1^2} \cos I$  is conserved at quadrupole order (e.g., [Lithwick & Naoz 2011](#)). But for our inverse problem, the fixed points ( $\omega_2 = \pm 90^\circ$ ,  $\dot{\omega}_2 = 0$ ) appear at fixed inclinations  $I$  of  $63^\circ$  and  $117^\circ$  that are independent of  $J_z$  (for  $e_1 = 0$ ). In this sense, the inverse Kozai resonance is “less flexible” than the conventional Kozai resonance.

The  $\omega_2$  resonance exists only in a narrow range of  $J_z$  that is specific to a given  $\alpha = a_1/a_2$ , as we have determined by numerical experimentation. Outside this range,  $\omega_2$  circulates and  $e_2$  and  $I$  hardly vary (Figure 1). Fine-tuning  $J_z$  can produce large resonant oscillation amplitudes in  $e_2$  and  $I$ ; some of these trajectories lead to orbit crossing with the perturber, as seen in the panel for  $J_z = 0.400$  in Figure 1.

### 3.1.1 Precession Timescales

To supplement (31), we list here for ease of reference the remaining equations of motion of the test particle, all to leading order, as derived by [Gallardo et al. \(2012\)](#) for the case  $e_1 = 0$ . We have verified that the disturbing function we have derived in Section 2 yields identical expressions:

$$\left. \frac{de_2}{dt} \right|_{\text{hex}, e_1=0} = + \frac{45}{512} \frac{m_1}{m_0} \left( \frac{a_1}{a_2} \right)^4 \frac{e_2 n_2}{(1 - e_2^2)^3} \times (5 + 7 \cos 2I) \sin^2 I \sin 2\omega_2 \quad (32)$$

$$\left. \frac{dI}{dt} \right|_{\text{hex}, e_1=0} = - \frac{45}{1024} \frac{m_1}{m_0} \left( \frac{a_1}{a_2} \right)^4 \frac{e_2^2 n_2}{(1 - e_2^2)^4} \times (5 + 7 \cos 2I) \sin 2I \sin 2\omega_2 \quad (33)$$

$$\left. \frac{d\Omega_2}{dt} \right|_{\text{quad}, e_1=0} = - \frac{3}{4} \frac{m_1}{m_0} \left( \frac{a_1}{a_2} \right)^2 \frac{n_2}{(1 - e_2^2)^2} \cos I \quad (34)$$

$$\left. \frac{d\varpi_2}{dt} \right|_{\text{quad}, e_1=0} = + \frac{3}{16} \frac{m_1}{m_0} \left( \frac{a_1}{a_2} \right)^2 \frac{n_2}{(1 - e_2^2)^2} (3 - 4 \cos I + 5 \cos 2I). \quad (35)$$

As equations (34) and (35) show, the magnitudes of the precession rates for  $\Omega_2$  and  $\varpi_2$  are typically similar to within order-unity factors. We define a fiducial secular precession period

$$t_{\text{prec}}^{\text{quad}, e_1=0} \sim \frac{2\pi}{n_2} \frac{m_0}{m_1} \left( \frac{a_2}{a_1} \right)^2 (1 - e_2^2)^2 \quad (36)$$

which reproduces the precession period for  $\Omega_2$  seen in the sample evolution of Figure 2 to within a factor of 3. The scaling factors in (36) are more reliable than the overall magnitude; the dependencies on  $m_0$ ,  $m_1$ ,  $a_1$ , and  $a_2$  can be used to scale the time coordinate of one numerical computation to another. Figure 2 is made for a particle in the inverse Kozai resonance; note how the oscillation periods for  $\omega_2$ , and by extension  $I$  and  $q_2$ , are each a few dozen times longer than the nodal precession period. This is expected since for the inverse Kozai resonance,  $d\omega_2/dt$  vanishes at quadrupole order, leaving the hexadecapole contribution, which is smaller by  $\sim (a_1/a_2)^2 = 1/25$ , dominant.

As shown in Figure 2, the secular trajectory within the  $\omega_2$  resonance is confirmed qualitatively by the  $N$ -body symplectic integrator WHFast ([Rein & Tamayo 2015](#);

[Wisdom & Holman 1991](#)), part of the REBOUND package (version 3.5.8; [Rein & Liu 2012](#)). A timestep of 0.25 yr was used (0.28% of the orbital period of the interior perturber) for the  $N$ -body integration shown; it took less than 3 wall-clock hours to complete the 5 Gyr integration using a 2.2 GHz Intel Core i7 processor on a 2015 MacBook Air laptop.

### 3.1.2 Inverse Kozai vs. Kozai

In the top panel of Figure 3, we show analogues to the “Kozai curves” made by [Lithwick & Naoz \(2011\)](#) for the conventional problem. This top panel delineates the allowed values of test particle eccentricity and inclination for given  $J_z$  and  $R$  when  $e_1 = 0$ . Contrast these “inverse Kozai curves” with the Kozai curves calculated by [Lithwick & Naoz \(2011\)](#) in their Figure 2 (left panel): for the inverse problem, the range of allowed eccentricities and inclinations is much more restricted (at fixed  $J_z$  and  $R$ ) than for the conventional problem. For the inverse problem when  $e_1 = 0$ ,  $e_2$  and  $I$  are strictly constant at quadrupole order; variations in  $e_2$  and  $I$  for the case of a circular perturber are possible starting only at hexadecapole order, via the small inverse Kozai resonant term in  $R$  proportional to  $e_2^2 \cos 2\omega_2$  (variations in  $\omega_2$  directly drive the variations in  $e_2$  and  $I$  when  $e_1 = 0$ ). By comparison, in the conventional problem, variations in test particle eccentricity and inclination are possible even at quadrupole order, and large.

This key difference between the conventional and inverse problems stems from the difference between the interior and exterior expansions of the  $1/\Delta$  potential. The conventional interior expansion involves the sum  $P_\ell r_{\text{test}}^\ell$ , where  $P_\ell$  is the Legendre polynomial of order  $\ell$  and  $r_{\text{test}}$  is the radial position of the test particle. The inverse exterior expansion involves a qualitatively different sum,  $P_\ell r_{\text{test}}^{-(\ell+1)}$ . The time-averaged potentials in the conventional and inverse problems therefore involve different integrals; what averages to a term proportional to  $\cos(2\omega_{\text{test}})$  in the conventional quadrupole problem averages instead in the inverse problem to a constant, independent of the test particle’s argument of periastron  $\omega_{\text{test}}$  (we have verified this last statement by evaluating these integrals). An interior multipole moment of order  $\ell$  is not the same as an exterior multipole moment of the same order. We could say that the inverse exterior potential looks “more Keplerian” insofar as its monopole term scales as  $1/r_{\text{test}}$ .

## 4 ECCENTRIC PERTURBER

When  $e_1 \neq 0$ , all orders (quadrupole, octopole, and hexadecapole) contribute to the potential seen by the test particle. The potential is no longer axisymmetric, and so  $J_z$  is no longer conserved. This opens the door to orbit “flipping”, i.e., a prograde ( $I < 90^\circ$ ) orbit can switch to being retrograde ( $I > 90^\circ$ ) and vice versa (e.g., [Naoz et al. 2017](#)). There is only one constant of the motion,  $R$ .

### 4.1 First Survey

Whereas when  $e_1 = 0$  the evolution did not depend on  $\Omega_2$ , it does when  $e_1 \neq 0$ . For our first foray into this

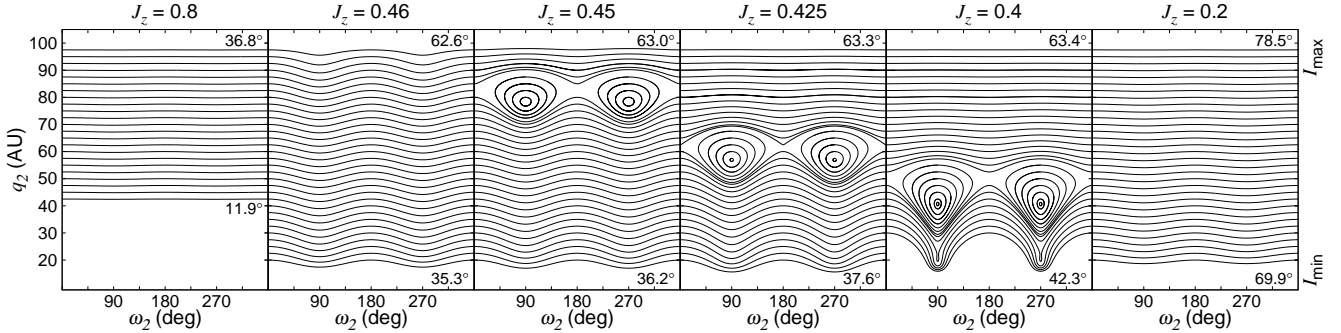


**Figure 1.** Periastron distances  $q_2$  vs. arguments of periastron  $\omega_2$ , for  $e_1 = 0$ . Because the potential presented by a circular perturber is axisymmetric,  $J_z = \sqrt{1 - e_2^2} \cos I$  is conserved; trajectories in a given panel have  $J_z$  as annotated. For given  $J_z$ , the inclination  $I$  increases monotonically but not linearly with  $q_2$ ; the maximum and minimum inclinations for the trajectories plotted are labeled on the right of each panel. In a narrow range of  $J_z = 0.40$ – $0.45$  (for our chosen  $\alpha = a_1/a_2 = 0.2$ ), the inverse Kozai (a.k.a.  $\omega_2$ ) resonance appears, near  $I \simeq 63^\circ$ . Near  $J_z = 0.40$ , the inverse Kozai resonance can force the test particle to cross orbits with the perturber.

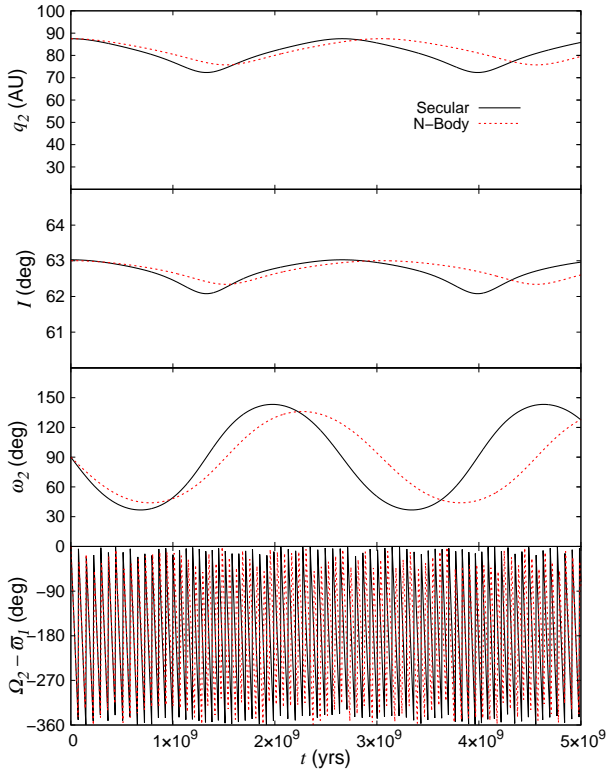


**Figure 2.** Time evolution within the inverse Kozai resonance. The trajectory chosen is the one in Figure 1 with  $J_z = 0.45$  and the largest libration amplitude. The nodal ( $\Omega_2$ ) precession arises from the quadrupole potential and is therefore on the order of  $1/a^2 \sim 25$  times faster than the libration timescale for  $\omega_2$ , which is determined by the hexadecapole potential. Initial conditions:  $\omega_2 = 90^\circ$ ,  $\Omega_2 = 0^\circ$ ,  $q_2 = 87.5$  AU,  $I = 63^\circ$ . Overplotted in red dashed lines are the results of an  $N$ -body integration with identical initial conditions (and initial true anomalies  $f_1 = 0^\circ$  and  $f_2 = 180^\circ$ ) inputted as Jacobi coordinates. The  $N$ -body integration is carried out using WHFast, part of the REBOUND package (Rein & Tamayo 2015; Wisdom & Holman 1991).

large multi-dimensional phase space, we divided up initial conditions as follows. For each of four values of  $e_1 \in \{0.03, 0.1, 0.3, 0.7\}$ , we scanned systematically through different initial values of  $q_{2,\text{init}}$  (equivalently  $e_{2,\text{init}}$ ) ranging between  $a_2 = 100$  AU and  $a_1 = 20$  AU. For each  $q_{2,\text{init}}$ , we assigned  $I_{\text{init}}$  according to one of three values of  $J_{z,\text{init}} \equiv \sqrt{1 - e_{2,\text{init}}^2} \cos I_{\text{init}} \in \{0.8, 0.45, 0.2\}$ , representing “low”, “intermediate”, and “high” inclination cases, broadly speaking. Having set  $e_1$ ,  $q_{2,\text{init}}$  ( $e_{2,\text{init}}$ ), and  $J_{z,\text{init}}$  ( $I_{\text{init}}$ ), we cycled through five values of  $\varpi_{2,\text{init}} \in \{0^\circ, 45^\circ, 90^\circ, 135^\circ, 180^\circ\}$  and three values of  $\omega_{2,\text{init}} \in \{0^\circ, 90^\circ, 270^\circ\}$ .

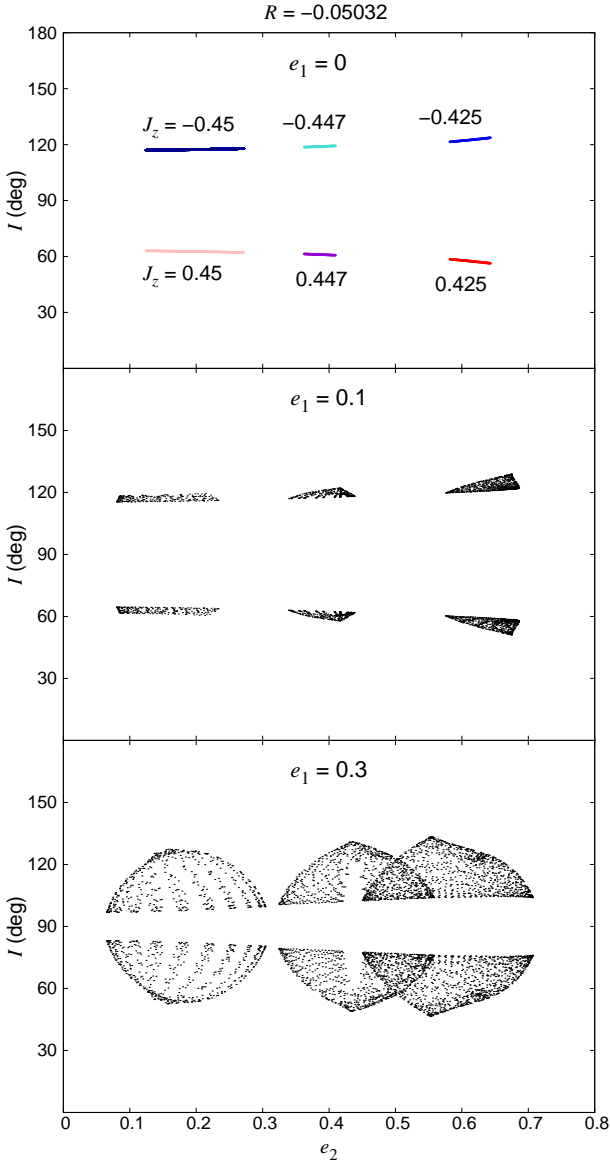
We studied all integrations from this large ensemble, adding more with slightly different initial conditions as our curiosity led us. In what follows, we present a subset of the results from this first survey, selecting those we thought representative or interesting. Later, in Section 4.2, we will provide a second and more thorough survey using surfaces of section. A few sample integrations from both surveys will be tested against  $N$ -body calculations in Section 4.3 (see also Figure 2).

#### 4.1.1 Low Perturber Eccentricity $e_1 \leq 0.1$

Comparison of Figure 4 with Figure 1 shows that at low perturber eccentricity,  $e_1 \lesssim 0.1$ , the test particle does not much change its behavior from when  $e_1 = 0$  (for a counter-example, see Figure 6). The same inverse Kozai resonance appears for  $J_{z,\text{init}} = 0.45$  and  $e_1 = 0.1$  as it does for  $e_1 = 0$ . The maximum libration amplitude of the resonance is somewhat higher at the larger  $e_1$ . The trajectories shown in Figure 4 are for  $\varpi_{2,\text{init}} = 0^\circ$ , but qualitatively similar results obtain for other choices of  $\varpi_{2,\text{init}}$ .

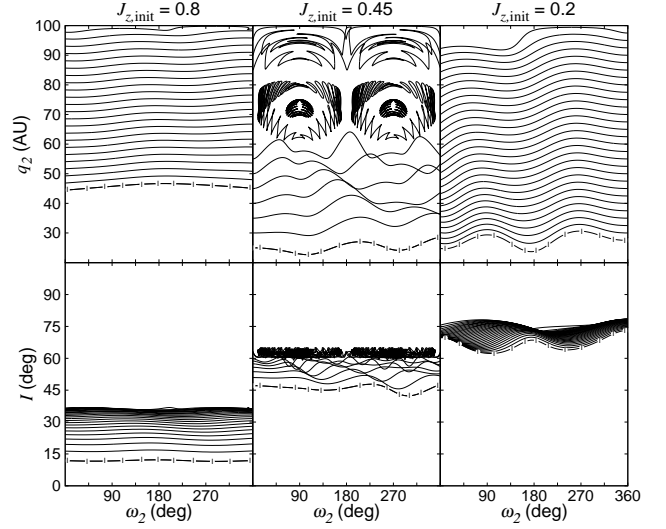
The middle panel of Figure 3 elaborates on this result, showing that even though  $J_{z,\text{init}}$  is not strictly conserved when  $e_1 \neq 0$ , it can be approximately conserved (again, see the later Figure 6 for a counter-example). Test particles explore more of  $e_2$ - $I$  space when  $e_1 = 0.1$  than when  $e_1 = 0$ , but they still largely respect (for the specific  $R$  of Figure 3) the constraints imposed by  $J_z$  when  $e_1 = 0$ . This statement also holds at  $e_1 = 0.3$  (lower panel), but to a lesser extent.

Figure 5 illustrates how the hexadecapole (hex) potential—specifically the inverse Kozai resonance—can



**Figure 3.** Inclination  $I$  vs. eccentricity  $e_2$  for a constant disturbing function  $R = -0.05032$  (see Section 2.1 for the units of  $R$ ). When  $e_1 = 0$ ,  $J_z$  is an additional constant of the motion; the resultant “inverse Kozai curves” (top panel) for our external test particle are analogous to the conventional “Kozai curves” shown in Figure 2 of Lithwick & Naoz (2011) for an internal test particle. Compared to the conventional case, the ranges of  $I$  and  $e_2$  in the inverse case are much more restricted; what variation there is is only possible because of the  $e_2^2 \cos(2\omega_2)$  term that appears at hexadecapolar order (see equation 22). As  $e_1$  increases above zero (middle and bottom panels),  $J_z$  varies more and variations in  $I$  grow larger. In each of the middle and bottom panels, points are generated by integrating the equations of motion for six sets of initial conditions specified in Table A1.

qualitatively change the test particle dynamics at octopole (oct) order. Only at hex order is the  $\omega_2$  resonance evident. Compared to the oct level dynamics, the periastron distance  $q_2$  varies more strongly, hitting its maximum and minimum values at  $\omega_2 = 90^\circ$  or  $270^\circ$  (instead of at  $0^\circ$  and  $180^\circ$ , as an oct treatment would imply).



**Figure 4.** Analogous to Figure 1, but now for a mildly eccentric perturber ( $e_1 = 0.1$ ). Because  $e_1 \neq 0$ ,  $J_z$  is not conserved and cannot be used to connect  $q_2$  and  $I$  uniquely; we have to plot  $q_2$  and  $I$  in separate panels. Nevertheless,  $e_1$  is still small enough that  $J_z$  is approximately conserved;  $q_2$  and  $I$  still roughly follow one another for a given  $J_{z,\text{init}}$ , i.e., the family of trajectories proceeding from lowest  $I$  (marked by vertical bars) to highest  $I$  corresponds to the same family of trajectories proceeding from lowest  $q_2$  (marked by vertical bars) to highest  $q_2$ . The  $\omega_2$  resonance can still be seen near  $I \approx 63^\circ$ , in the center panels for  $J_{z,\text{init}} = 0.45$ . All the non-resonant trajectories are initialized with  $\varpi_2 = 0^\circ$  and  $\omega_2 = 0^\circ$ . For the four resonant trajectories, the initial  $\varpi_2 = 0^\circ$  and  $\omega_2 = \pm 90^\circ$ .

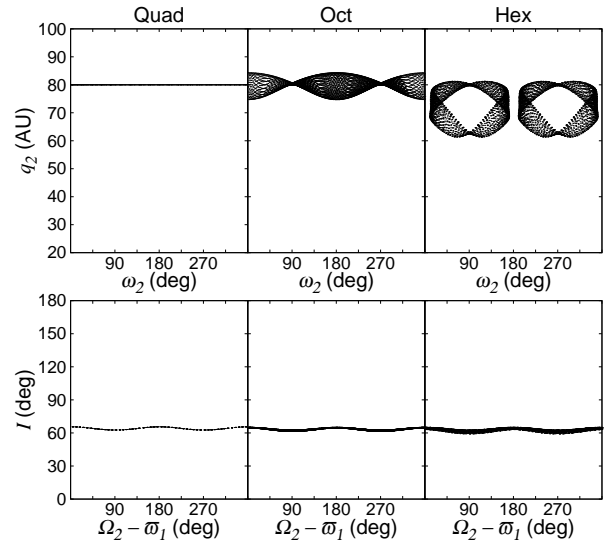


**Figure 5.** Comparing quadrupole (quad), octopole (oct), and hexadecapole (hex) evolutions for  $e_1 = 0.1$  and  $\varpi_1 = 0^\circ$  and the same test particle initial conditions ( $e_2 = 0.2$ ,  $I = 62.66^\circ$ ,  $\varpi_2 = 0^\circ$ , and  $\omega_2 = 90^\circ$ ). The hex panel features a second set of initial conditions identical to the first except that  $\omega_2 = 270^\circ$ ; the two hex trajectories map to the same quad and oct trajectories as shown. The inverse Kozai resonance, featuring libration of  $\omega_2$  about  $\pm 90^\circ$  and  $\sim 20\%$  variations in  $e_2$ , appears only in a hex-level treatment.

Orbit flipping becomes possible when  $e_1 \neq 0$ , for sufficiently large  $I$  or  $e_2$  (Naoz et al. 2017). Figure 6 is analogous to Figure 3 except that it is made for a more negative  $R$ , corresponding to larger  $I$  (insofar as  $R$  is dominated by the quadrupole term). For this  $R = -0.1373$ , as with the previous  $R = -0.05032$ ,  $e_2$  and  $I$  hardly vary when  $e_1 = 0$  (Section 3.1.2). But when  $e_1 = 0.1$ , the constraints imposed by fixed  $J_z$  come loose; Figure 6 shows that a single particle's  $J_z$  can vary dramatically from positive (prograde) to negative (retrograde) values. As shown by Naoz et al. (2017, see their Figure 1), such orbit flipping is possible even at quadrupole order; flipping is not associated with the  $\omega_2$  resonance, but rather with librations of  $\Omega_2 - \varpi_1$  about  $90^\circ$  or  $270^\circ$ . We verify the influence of this  $\Omega_2 - \varpi_1$  resonance in the middle panel of Figure 6.

#### 4.1.2 High Perturber Eccentricity $e_1 = 0.3, 0.7$

We highlight a few comparisons between an oct level treatment and a hex level treatment. We begin with Figure 7 which shows practically no difference. Many of the integrations in our first survey showed no significant difference in going from oct to hex. We also tested some of the cases showcased in Naoz et al. (2017) and found that including the hex dynamics did not substantively alter their evolution.

Cases where the hex terms matter are shown in Figures 8–11. The  $\omega_2$  resonance, seen only at hex order, can stabilize the motion; in Figure 8, the  $\omega_2$  resonance eliminates the chaotic variations seen at the oct level in  $q_2$  and  $I$ . Even when the  $\omega_2$  resonance is not active, hex level terms can dampen eccentricity and inclination variations (Figures 9 and 10). But the hex terms do not necessarily suppress; in Figure 11 they are seen to nudge the test particle from a prograde to a retrograde orbit, across the separatrix of the  $\Omega_2 - \varpi_1$  resonance.

## 4.2 Second Survey: Surfaces of Section

Surfaces of section (SOS's) afford a more global (if also more abstract) view of the dynamics. By plotting the test particle's position in phase space only when one of its coordinates periodically equals some value, we thin its trajectory out, enabling it to be compared more easily with the trajectories of other test particles with different initial conditions. In this lower dimensional projection, it is also possible to identify resonances, and to distinguish chaotic from regular trajectories.

Since we are particularly interested in seeing how  $\omega_2$  and its quasi-conjugate  $e_2$  behave, we section using  $\Omega_2$ , plotting the particle's position in  $q_2$ - $\omega_2$  space and  $I$ - $\omega_2$  space whenever  $\Omega_2 = 180^\circ$  (with zero longitude defined by  $\varpi_1 = 0^\circ$ ), regardless of the sign of  $\dot{\Omega}_2$ . A conventional SOS would select for  $\dot{\Omega}_2$  of a single sign, but in practice there is no confusion; prograde orbits all have  $\dot{\Omega}_2 < 0$  (see equation 34) while retrograde orbits have  $\dot{\Omega}_2 > 0$ ; we focus for simplicity on prograde orbits and capture a few retrograde branches at the smallest values of  $R$  (see the rightmost panels of Figures 12–14). We have verified in a few cases that the trajectories so plotted trace the maximum and minimum values of  $q_2$  and  $I$ ; our SOS's contain the bounding envelopes of the trajectories.

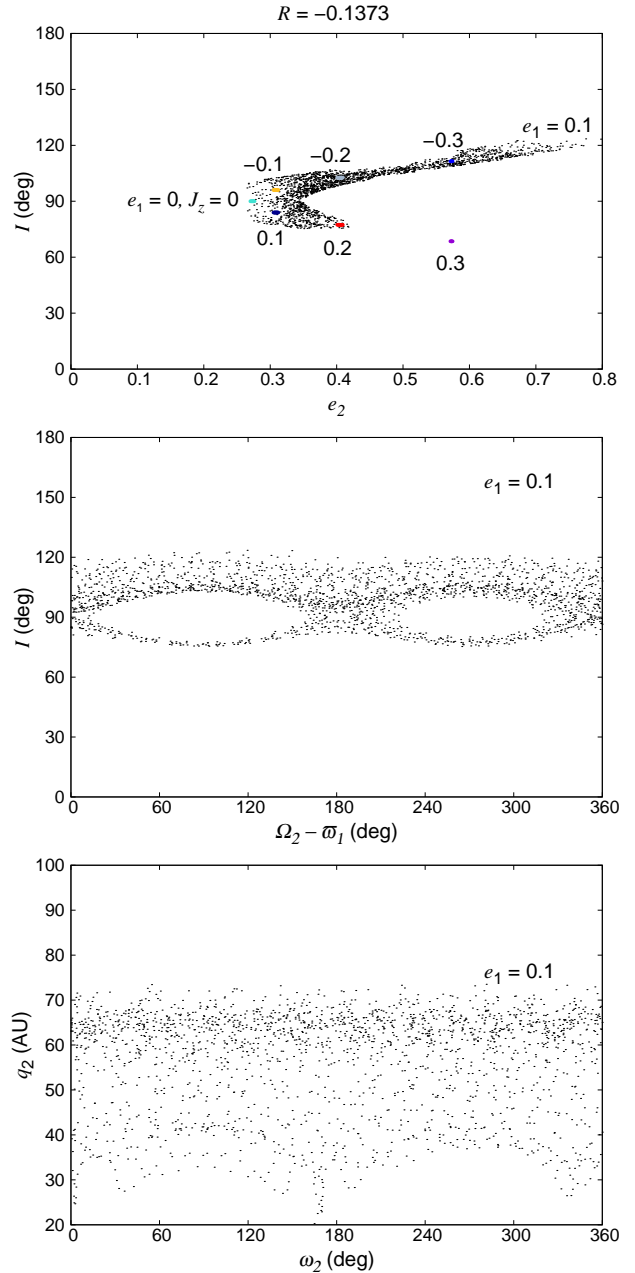


**Figure 6.** Top panel: Inclination  $I$  vs. eccentricity  $e_2$  for a fixed disturbing function  $R = -0.1373$  (see Section 2.1 for the units of  $R$ ). Different colored points, corresponding to different  $J_z$  values as marked, are for  $e_1 = 0$ , and are analogous to those shown in the top panel of Figure 3. The black points represent the trajectory of a single test particle, integrated for  $e_1 = 0.1$  and using the following initial conditions:  $e_2 = 0.3691$ ,  $I = 85^\circ$ ,  $\varpi_2 = 0^\circ$ , and  $\Omega_2 = 0^\circ$ . When  $e_1 \neq 0$ ,  $J_z$  is no longer conserved, and  $e_2$  and  $I$  vary dramatically for this value of  $R$ ;  $J_z$  even changes sign as the orbit flips. The variation in  $e_2$  is so large that eventually the test particle crosses the orbit of the perturber ( $e_2 > 0.8$ ), at which point we terminate the trajectory. Center panel: Inclination  $I$  vs. longitude of ascending node  $\Omega_2$  (referenced to  $\varpi_1$ , the periape longitude of the perturber) for the same black trajectory shown in the top panel. The two lobes of the  $\Omega_2 - \varpi_1$  resonance (Naoz et al. 2017), around which the particle lingers, are visible. Bottom panel: The same test particle trajectory shown in black for the top and middle panels, now in  $q_2$  vs.  $\omega_2$  space. The evolution is evidently chaotic.



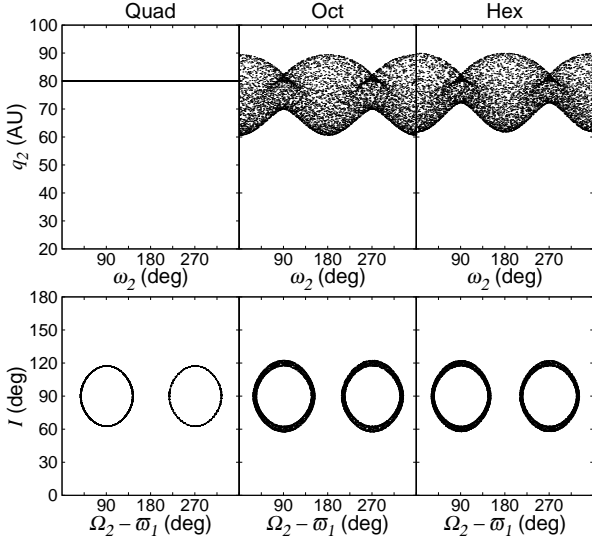


**Figure 7.** Analogous to Figure 5, but for  $e_1 = 0.3$  and the following test particle initial conditions:  $e_2 = 0.2$ ,  $I = 62.66^\circ$ ,  $\Omega_2 = \pm 90^\circ$ ,  $\varpi_2 = 0^\circ$ . The two test particle trajectories overlap in  $q_2 - \omega_2$  space (top panels). For these initial conditions, the  $\Omega_2 - \varpi_1$  resonance (Naoz et al. 2017) appears at all orders quad through hex (bottom panels). The oct and hex trajectories appear qualitatively similar in all respects.

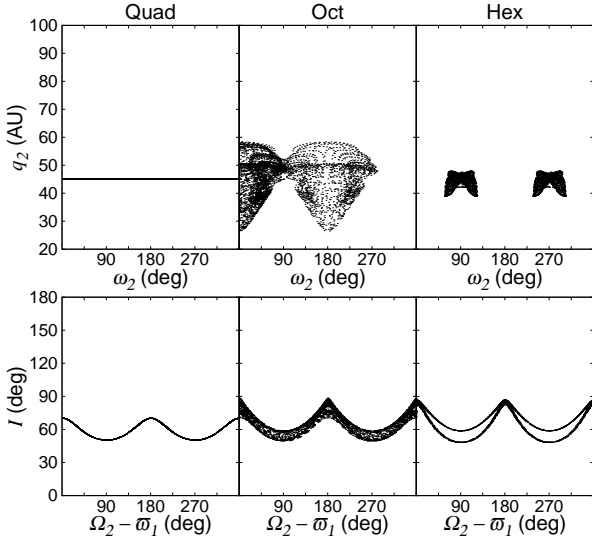


**Figure 8.** Analogous to Figure 5, but for  $e_1 = 0.3$  and  $\varpi_1 = 0^\circ$  and the following test particle initial conditions:  $e_2 = 0.55$ ,  $I = 57.397^\circ$ ,  $\Omega_2 = 45^\circ$  and  $225^\circ$ ,  $\varpi_2 = 135^\circ$ . The inverse Kozai ( $\omega_2$ ) resonance is visible in the hex panels only, with a more widely varying inclination here for  $e_1 = 0.3$  than for  $e_1 = 0$  (compare with Figure 5). The phase space available to the  $\omega_2$  resonance shrinks with increasing  $e_1$ ; at  $e_1 = 0.7$ , we could not find the resonance (see Figure 14). Two test particle trajectories are displayed for the hex panel; since they overlap at the quad and oct levels, only one trajectory is shown for those panels (the one for which the initial  $\Omega_2 = 45^\circ$ ).

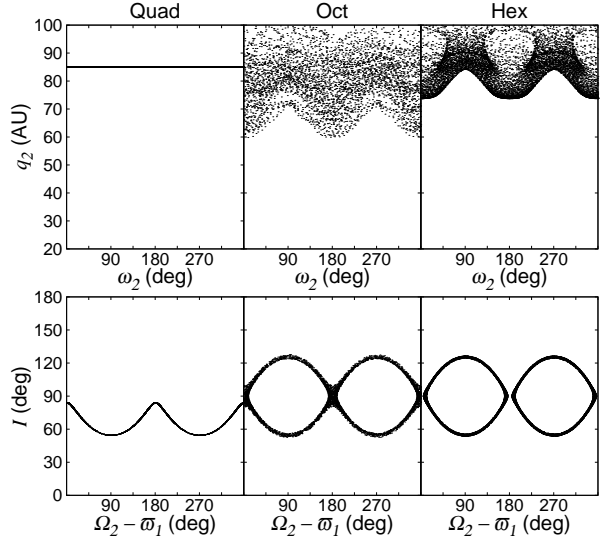


**Figure 9.** Analogous to Figure 5, but for  $e_1 = 0.3$  and  $\varpi_1 = 0^\circ$  and the following test particle initial conditions:  $e_2 = 0.15$ ,  $I = 62.925^\circ$ ,  $\Omega_2 = 45^\circ$  and  $225^\circ$ ,  $\varpi_2 = 135^\circ$ . Two test particle trajectories are displayed for the hex panel; since they overlap at the quad and oct levels, only one trajectory is shown for those panels (the one for which the initial  $\Omega_2 = 225^\circ$ ). The hex potential suppresses the eccentricity variation seen at the oct level, and removes the particle from the separatrix of the  $\Omega_2$  resonance, bringing it onto one of two islands of libration.

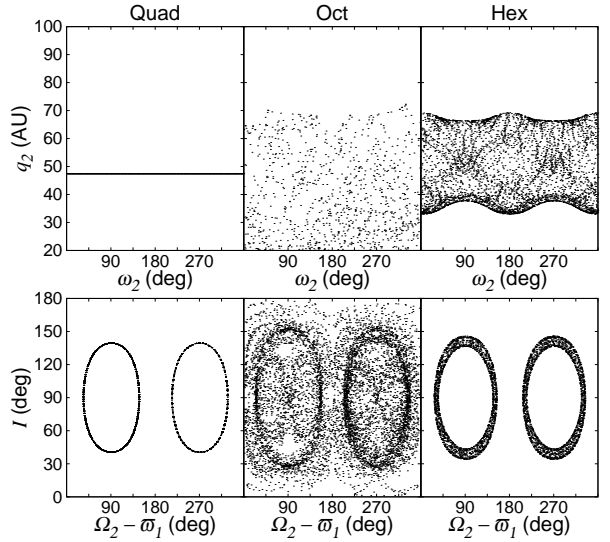


**Figure 10.** Analogous to Figure 5, but for  $e_1 = 0.7$  and  $\varpi_1 = 0^\circ$  and the following test particle initial conditions:  $e_2 = 0.525$ ,  $I = 58.081^\circ$ ,  $\Omega_2 = 135^\circ$  and  $315^\circ$ ,  $\varpi_2 = 135^\circ$ . As with Figures 8 and 9, the hex potential helps to stabilize the motion; here it locks the particle to one of two librating islands of the  $\Omega_2$  resonance and prevents the orbit crossing seen at the oct level.

Figure 12 shows  $\Omega_2$ -SOS's for  $e_1 = 0.1$  and a sequence of  $R$ 's (including those  $R$  values used for Figures 3 and 6). At the most positive  $R$  (lowest  $I$ ), the trajectories are regular, with small-amplitude variations in  $q_2$  and  $I$ . At more negative  $R$  (larger  $I$ ), three strong resonances appear, each characterized by substantial variations in  $q_2$ :

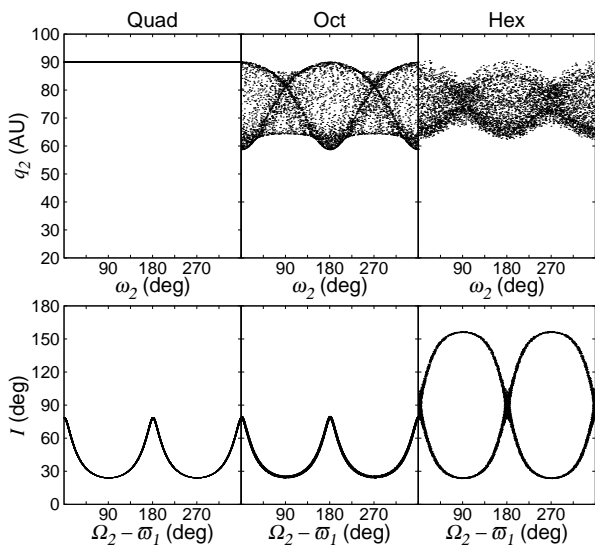


**Figure 11.** Analogous to Figure 5, but for  $e_1 = 0.7$  and  $\varpi_1 = 0^\circ$  and the following test particle initial conditions:  $e_2 = 0.1$ ,  $I = 84.232^\circ$ ,  $\Omega_2 = 180^\circ$ ,  $\varpi_2 = 180^\circ$ . Here the hex potential nudges the particle from a circulating trajectory onto the separatrix of the  $\Omega_2 - \varpi_1$  resonance (contrast with Figures 9 and 10).

(i) The first of these (appearing at  $R = +0.0721$ , second panel from left) is an “apse-aligned” resonance for which  $\varpi_2 - \varpi_1$  librates about  $0^\circ$  and

$$I(\varpi_2 - \varpi_1 - \text{res}) \simeq \arccos\left(\frac{+1 \pm \sqrt{6}}{5}\right) \simeq 46^\circ \text{ and } 107^\circ. \quad (37)$$

At these inclinations, by equation (35),  $d\varpi_2/dt|_{\text{quad}, e_1=0} = 0$ .<sup>4</sup>

(ii) The second of the resonances ( $R = -0.0721$ , two lobes in the middle panel) is the inverse Kozai or  $\omega_2$  resonance, appearing at  $I(\omega_2 - \text{res}) \simeq 63^\circ$  and  $117^\circ$ , and for which  $\omega_2$  librates about  $\pm 90^\circ$  (Section 3.1).

(iii) The third resonance ( $R = -0.0721$ ,  $-0.0938$ , and  $-0.1373$ ; middle, fourth, and fifth panels) appears at

$$I(\varpi_2 + \varpi_1 - 2\Omega_2 - \text{res}) \simeq \arccos\left(\frac{-1 \pm \sqrt{6}}{5}\right) \simeq 73^\circ \text{ and } 134^\circ, \quad (38)$$

inclinations for which  $d(\varpi_2 + \varpi_1 - 2\Omega_2)/dt = 0$  or equivalently  $\dot{\omega}_2 = \dot{\Omega}_2$  (equations 31 and 34). The resonant angle  $\varpi_2 + \varpi_1 - 2\Omega_2 (= \omega_2 - \Omega_2)$  librates about  $0^\circ$ .<sup>5</sup>

For the above three resonances, we have verified that

<sup>4</sup> The apse-aligned resonance identified here is at small  $\alpha$  and large  $I \simeq 46^\circ/107^\circ$ , but another apse-aligned resonance also exists for orbits that are co-planar or nearly so (e.g., Wyatt et al. 1999). The latter can be found using Laplace-Lagrange secular theory (e.g., Murray & Dermott 2000), which does not expand in  $\alpha$  but rather in eccentricity and inclination; it corresponds to a purely forced trajectory with no free oscillation. Laplace-Lagrange (read: low-inclination secular) dynamics are well understood so we do not discuss them further.

<sup>5</sup> The analogue of this resonance for the interior test particle problem has been invoked, together with other secular and mean-motion resonant effects, in the context of Planet Nine and Centaur evolution (Batygin & Morbidelli 2017).

their respective resonant arguments ( $\varpi_2 - \varpi_1$ ;  $\omega_2$ ;  $\varpi_2 + \varpi_1 - 2\Omega_2$ ) librate (see also Figure 15), and have omitted their retrograde branches from the SOS for simplicity. The  $\varpi_2 + \varpi_1 - 2\Omega_2$  and  $\varpi_2 - \varpi_1$  resonances appear at octopole order; they are associated with the first two terms in the octopole disturbing function (21), respectively. The  $\omega_2$  resonance is a hexadecapolar effect, as noted earlier.

The SOS for  $e_1 = 0.3$  (Figure 13) reveals dynamics qualitatively similar to  $e_1 = 0.1$ , but with larger amplitude variations in  $q_2$ . We have verified in Figure 13 that the island of libration seen at  $R = 0.0503$  is the  $\varpi_2 - \varpi_1$  resonance; that the islands near the top of the panels for  $R = 0$  and  $-0.0503$  represent the  $\varpi_2 + \varpi_1 - 2\Omega_2$  resonance; and that the two islands centered on  $\omega_2 = \pm 90^\circ$  at  $R = -0.0503$  represent the inverse Kozai resonance.

For both  $e_1 = 0.3$  and  $0.1$ , chaos is more prevalent at more negative  $R$  / larger  $I$ . The chaotic trajectories dip to periastron distances  $q_2$  near  $a_1 = 20$  AU, and in Figure 12 we show a few that actually cross orbits with the perturber (the gray trajectory for  $R = -0.0938$  is situated near the separatrix of the inverse Kozai resonance: the two resonant lobes are seen in ghostly outline). The orbit-crossing behavior seen in Figure 12 occurs late in the test particle’s evolution—in fact, at times longer than the age of the universe for our parameter choices! We nevertheless show these trajectories because the evolutionary timescales shorten and become realistic for smaller  $a_1$  and  $a_2$  (Section 3.1.1). Unfortunately, no matter how we scale  $a_1$  and  $a_2$ , the computational cost of finding  $N$ -body counterparts to the orbit-crossing trajectories of Figure 12 is necessarily expensive because the  $N$ -body timestep scales with the orbital period of the interior body;  $N$ -body tests of these particular trajectories are deferred to future work.

At  $e_1 = 0.7$  (Figure 14) we find, in addition to the  $\varpi_2 - \varpi_1$  resonance at  $R \leq 0.4$ , a new resonance at  $R \geq 0.5$ . For this latter resonance,  $\varpi_2 - 3\varpi_1 + 2\Omega_2 = \omega_2 + 3\Omega_2$  librates about  $0^\circ$ . Although this resonance is found at octopole order—it is embodied in the fourth term in equation (21)—we found by experimentation that eliminating the hexadecapole contribution to the disturbing function removes the test particle from this resonance (for the same initial conditions as shown in Figure 14). Evidently the hexadecapole potential helps to enforce  $\dot{\omega}_2 = -3\dot{\Omega}_2$  so that this octopole resonance can be activated. Remarkably, this  $\varpi_2 - 3\varpi_1 + 2\Omega_2$  resonance enables the test particle to cycle between a nearly (but not exactly) co-planar orbit to one inclined by  $\sim 60$ – $70^\circ$ , while having its eccentricity  $e_2$  vary between  $\sim 0.2$ – $0.6$ . We will see in Section 4.3, however, that a full  $N$ -body treatment mutes the effects of this resonance.

### 4.3 $N$ -Body Tests

Having identified five resonances in the above surveys, we test how robust they are using  $N$ -body integrations. We employ the WHFast symplectic integrator (Rein & Tamayo 2015; Wisdom & Holman 1991), part of the REBOUND package (Rein & Liu 2012), adopting timesteps between 0.1–0.25 yr. Initial conditions (inputted for the  $N$ -body experiments as Jacobi elements, together with initial true anomalies  $f_1 = 0^\circ$  and  $f_2 = 180^\circ$ ) were drawn from the above surveys with the goal of finding resonant libration at as large a perturber eccentricity  $e_1$  as possible. In Figure 15 we verify that the  $\omega_2$ ,

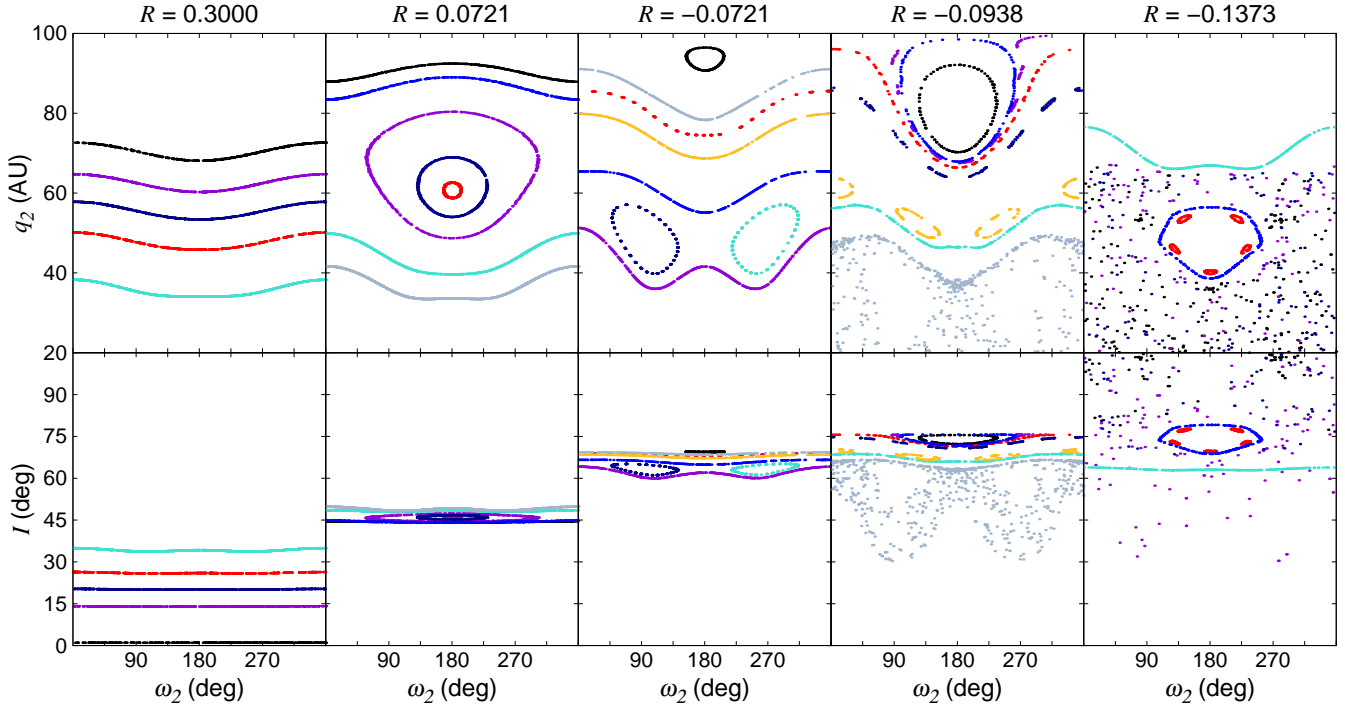


**Figure 12.** Surfaces of section (SOS's) for perturber eccentricity  $e_1 = 0.1$  and  $\varpi_1 = 0^\circ$  and various values of the disturbing function  $R$  (the only constant of the motion when  $e_1 \neq 0$ ; see Section 2.1 for the units of  $R$ ) labeled at the top of the figure. These SOS's are sectioned using  $\Omega_2$ : a point is plotted every time  $\Omega_2$  crosses  $180^\circ$ , irrespective of the sign of  $\dot{\Omega}_2$  (see text). Each test particle trajectory is assigned its own color; see Table A2 in the Appendix for the initial conditions. At  $R = 0.072$ , the  $\varpi_2 - \varpi_1$  resonance appears. At  $R = -0.0721$ , the  $\omega_2$  (inverse Kozai) resonance appears (dark blue and turquoise lobes centered on  $\omega_2 = \pm 90^\circ$ ). At  $R = 0, -0.0938$ , and  $-0.1373$ , the  $\varpi_2 + \varpi_1 - 2\Omega_2$  resonance manifests (this angle librates about  $0^\circ$ ). These three resonances are accessed at inclinations  $I \sim 45^\circ - 75^\circ$  (and at analogous retrograde inclinations that are not shown). The region at large  $q_2$  for  $R = -0.1373$  is empty because here the test particle locks into the  $\Omega_2 - \varpi_1$  resonance studied by Naoz et al. (2017), in which  $\Omega_2 - \varpi_1$  librates about  $90^\circ$  and so does not trigger our sectioning criterion.

$\Omega_2 - \varpi_1$ ,  $\varpi_2 - \varpi_1$ , and  $\varpi_2 + \varpi_1 - 2\Omega_2$  resonances survive a full  $N$ -body treatment when  $e_1$  is as high as 0.1, 0.7, 0.7, and 0.1, respectively (see also Figure 2). Table A5 records the initial conditions.

We were unable in  $N$ -body calculations to lock the test particle into the  $\varpi_2 - 3\varpi_1 + 2\Omega_2$  ( $= \omega_2 + 3\Omega_2$ ) resonance, despite exploring the parameter space in the vicinity where we found it in the secular surfaces of section. This is unsurprising insofar as we had found this particular resonance to depend on both octopole and hexadecapolar effects at the largest perturber eccentricity tested,  $e_1 = 0.7$ ; at such a high eccentricity, effects even higher order than hexadecapole are likely to be significant, and it appears from our  $N$ -body calculations that they are, preventing a resonant lock. We show in Figure 15 an  $N$ -body trajectory that comes close to being in this resonance (on average,  $\dot{\omega}_2 \approx -2.7\dot{\Omega}_2$ ). Although the inclination does not vary as dramatically as in the truncated secular evolution, it can still cycle between  $\sim 20^\circ$  and  $70^\circ$ .

The agreement between the  $N$ -body and secular integrations shown in Figure 15 is good, qualitatively and even quantitatively in some cases. We emphasize that these trajectories have not been cherry-picked to display such agreement; the initial conditions were drawn from the preceding surveys for the purpose of testing which resonances survive an  $N$ -body treatment. In the cases of the  $\Omega_2 - \varpi_1$  and  $\varpi_2 - \varpi_1$  resonances, the secular trajectories show amplitude modula-

tion/beating not seen in their  $N$ -body counterparts. Similar behavior was reported by Naoz et al. (2017, see their Figure 12). A broader continuum of forcing frequencies must be present at our standard value of  $\alpha = 0.2$  than is captured by our hex-limited treatment; certainly we obtain better agreement with  $N$ -body calculations at lower values of  $\alpha$  (as we have explicitly verified by testing, e.g.,  $\alpha = 0.05$  for the parameters of Figure 15c).

## 5 SUMMARY

We have surveyed numerically the dynamics of an external test particle in the restricted, secular, three-body problem. We wrote down the secular potential of an internal perturber to hexadecapolar order (where the expansion parameter is the ratio of semimajor axes of the internal and external bodies,  $\alpha = a_1/a_2 < 1$ ) by adapting the disturbing function for an external perturber as derived by Yokoyama et al. (2003, Y03). In making this adaptation, we corrected a misprint in the hexadecapolar potential of Y03 (M. Čuk 2017, personal communication). Our numerical survey was conducted at fixed  $\alpha = 0.2$ , the largest value we thought might still be captured by a truncated secular expansion (lower values generally do better).

Inclination variations for an external test particle can

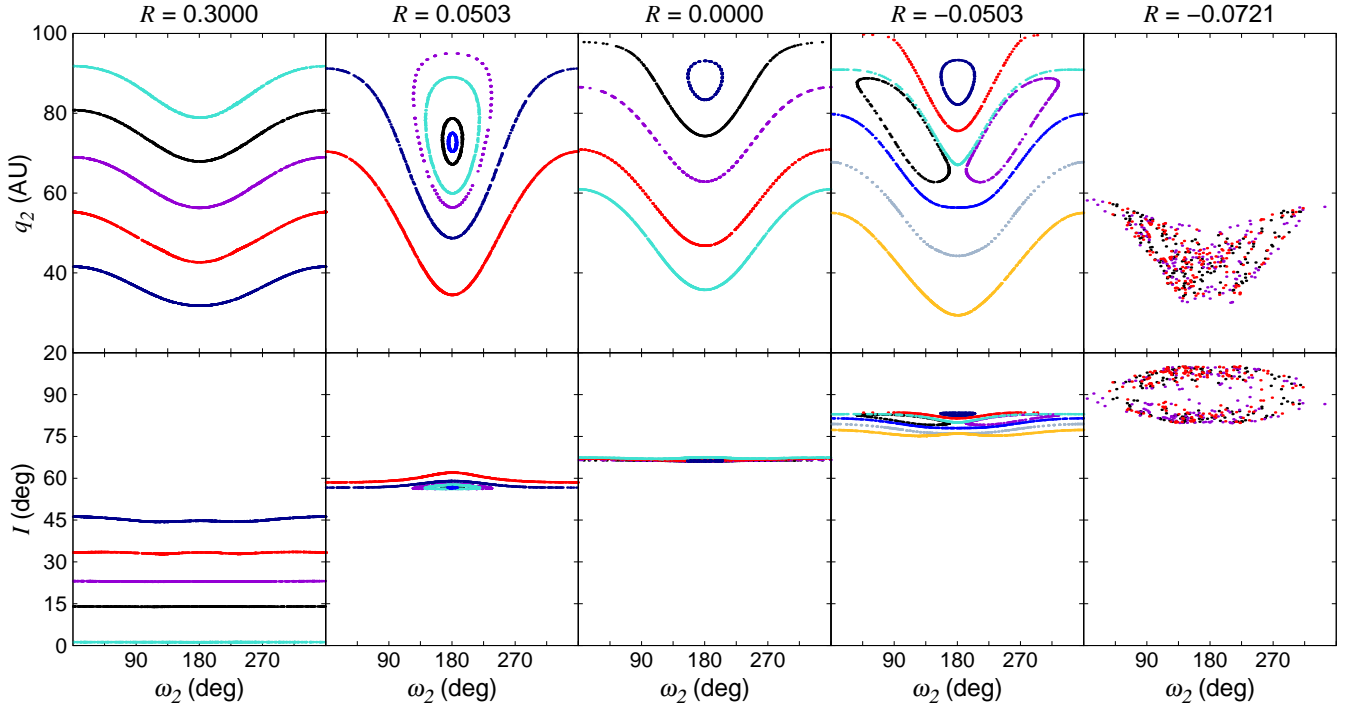


**Figure 13.** Same as Figure 12 but for  $e_1 = 0.3$ . The  $\varpi_2 - \varpi_1$  resonance appears at  $R = 0.0503$ ; the  $\varpi_2 + \varpi_1 - 2\Omega_2$  resonance appears at  $R = 0$  and  $-0.0503$ ; and the double-lobed inverse Kozai resonance appears at  $R = -0.0503$ . Initial conditions used to make this figure are in Table A3.

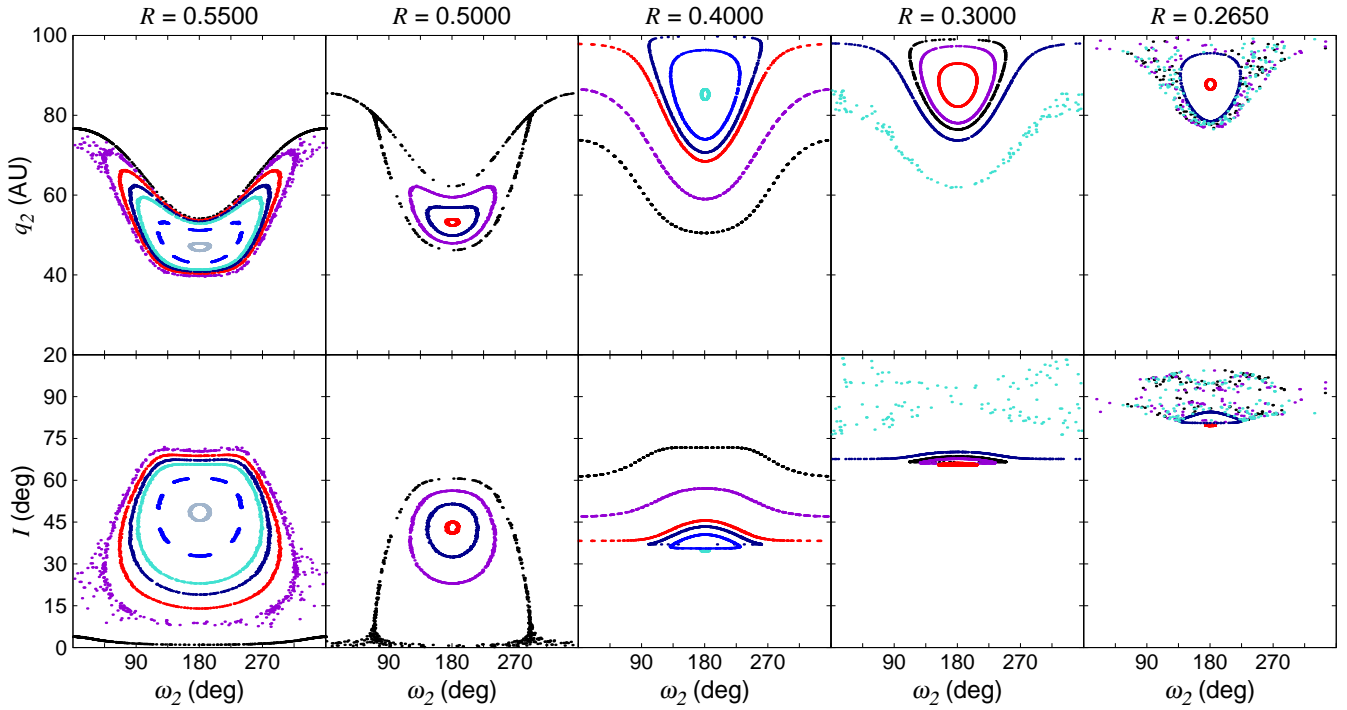


**Figure 14.** Same as Figure 12 but for  $e_1 = 0.7$ . In addition to the  $\varpi_2 - \varpi_1$  resonance at  $R \leq 0.4$ , a new resonance appears at  $R \geq 0.5$  for which  $\varpi_2 - 3\varpi_1 + 2\Omega_2 (= \varpi_2 + 3\Omega_2)$  librates about  $0^\circ$ . This last resonance, however, is not found in full  $N$ -body integrations (by contrast to the other four resonances identified in this paper; see Figure 15). Initial conditions used to make this figure are in Table A4.

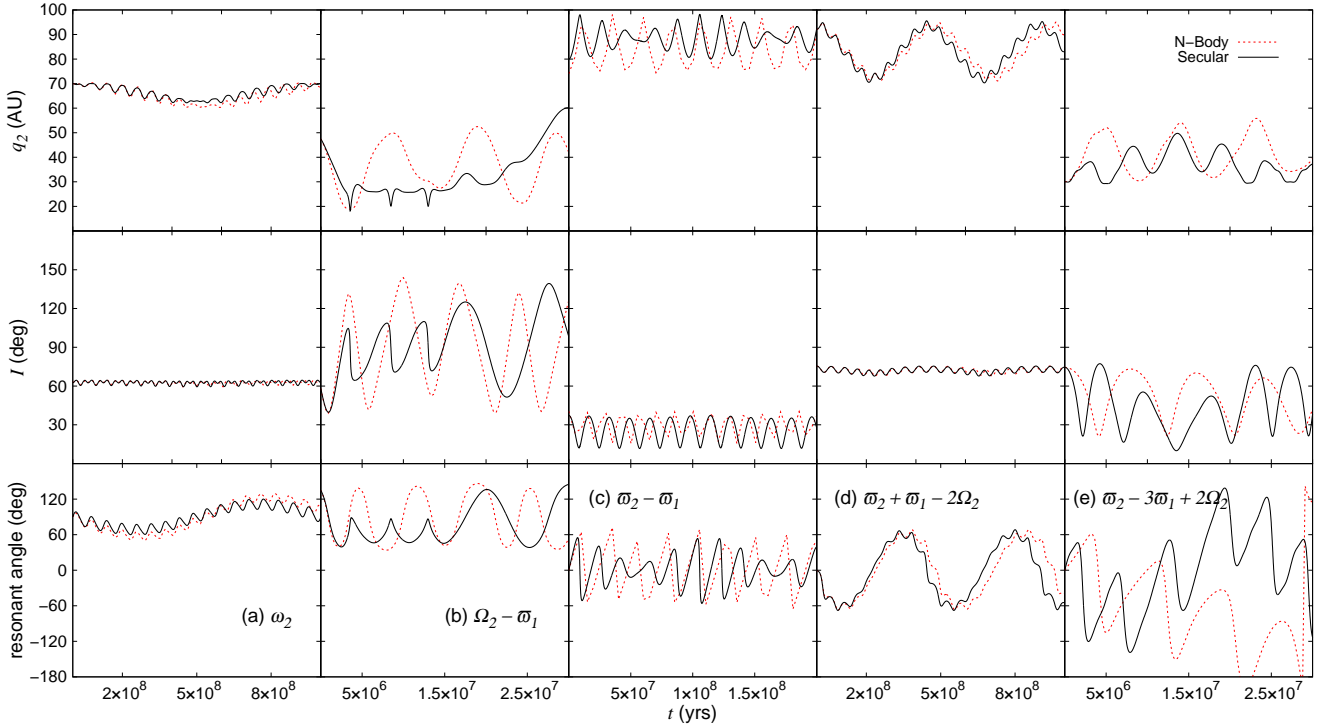


**Figure 15.** Comparison of  $N$ -body (dashed red) vs. secular (solid black) integrations. Initial conditions, summarized in Table A5, are chosen to lock the test particle into the  $\omega_2$ ,  $\Omega_2 - \varpi_1$ ,  $\varpi_2 - \varpi_1$ , and  $\varpi_2 + \varpi_1 - 2\Omega_2$  resonances (panels a through d). We failed to obtain a lock for the  $\varpi_2 - 3\varpi_1 + 2\Omega_2 = \omega_2 + 3\Omega_2$  resonance in our  $N$ -body calculations and offer an instead an  $N$ -body trajectory that comes close to librating ( $\dot{\omega}_2 \approx -2.7\Omega_2$ ; panel e), together with its secular counterpart which does appear to librate.

be dramatic when the eccentricity of the internal perturber  $e_1$  is non-zero. The variations in mutual inclination  $I$  are effected by a quadrupole resonance for which  $\Omega_2$ , the test particle’s longitude of ascending node (referenced to the orbit plane of the perturber, whose periape is at longitude  $\varpi_1$ ), librates about  $\varpi_1 \pm 90^\circ$ . Within this  $\Omega_2 - \varpi_1$  resonance, the test particle’s orbit flips (switches from prograde to retrograde). Flipping is easier—i.e., the minimum  $I$  for which flipping is possible decreases—with increasing  $e_1$ . All of this inclination behavior was described by Naoz et al. (2017; see also Verrier & Evans 2009 and Farago & Laskar 2010) and we have confirmed these essentially quadrupolar results here.

Eccentricity variations for an external test particle rely on octopole or higher-level effects (at the quadrupole level of approximation, the test particle eccentricity  $e_2$  is strictly constant). When  $e_1 = 0$ , octopole effects vanish, and the leading-order resonance able to produce eccentricity variations is the hexadecapolar “inverse Kozai” resonance in which the test particle’s argument of periastron  $\omega_2$  librates about  $\pm 90^\circ$  (Gallardo et al. 2012). The resonance demands rather high inclinations,  $I \approx 63^\circ$  or  $117^\circ$ . By comparison to its conventional Kozai counterpart which exists at quadrupole order, the hexadecapolar inverse Kozai resonance is more restricted in scope: it exists only over a narrow range of  $J_z = \sqrt{1 - e_2^2} \cos I$  for a given  $\alpha$ , and produces eccentricity variations on the order of  $\Delta e_2 \approx 0.2$ . For suitable  $J_z$  it can, however, lead to orbit-crossing with the perturber. In our truncated secular treatment, we found the inverse Kozai resonance to persist up to perturber eccentricities of  $e_1 = 0.3$ ;

in  $N$ -body experiments, we found the resonance only up to  $e_1 = 0.1$ . At higher  $e_1$ , the hexadecapolar resonance seems to disappear, overwhelmed by octopole effects.

Surfaces of section made for  $e_1 \neq 0$  and  $\Omega_2 = 180^\circ$  revealed two octopole resonances characterized by stronger eccentricity variations of  $\Delta e_2$  up to 0.5. The resonant angles are the apsidal difference  $\varpi_2 - \varpi_1$ , which librates about  $0^\circ$ , and  $\varpi_2 + \varpi_1 - 2\Omega_2$ , which also librates about  $0^\circ$ . The  $\varpi_2 - \varpi_1$  and  $\varpi_2 + \varpi_1 - 2\Omega_2$  resonances are like the inverse Kozai resonance in that they also require large inclinations,  $I \approx 46^\circ/107^\circ$  and  $73^\circ/134^\circ$ , respectively. The apse-aligned  $\varpi_2 - \varpi_1$  resonance survives full  $N$ -body integrations up to  $e_1 = 0.7$ ; the  $\varpi_2 + \varpi_1 - 2\Omega_2$  resonance survives up to  $e_1 = 0.1$ . At large  $e_1$ , the requirement on  $I$  for the  $\varpi_2 - \varpi_1$  resonance lessens to about  $\sim 20^\circ$ .

We outlined two rough, qualitative trends: (1) the larger  $e_1$  is, the more the eccentricity and inclination of the test particle can vary; and (2) the more polar the test particle orbit (i.e., the closer  $I$  is to  $90^\circ$ ), the more chaotic its evolution.

In some high-inclination trajectories—near the separatrix of the inverse Kozai resonance, for example—test particle periastra could be lowered from large distances to near the perturber. These secular channels of transport need to be confirmed with  $N$ -body tests.

This paper is but an initial reconnaissance of the external test particle problem. How the various resonances we have identified may have operated in practice to shape actual planetary/star systems is left for future study. In ad-

dition to more  $N$ -body tests, we also need to explore the effects of general relativity (GR). For our chosen parameters, GR causes the periapse of the perturber to precess at a rate that is typically several hundreds of times slower than the rate at which the test particle's node precesses. Such an additional apsidal precession is not expected to affect our results materially; still, a check should be made. A way to do that comprehensively is to re-compute our surfaces of section with GR.

## ACKNOWLEDGEMENTS

We are grateful to Edgar Knobloch and Matthias Reinisch for teaching Berkeley's upper-division mechanics course Physics 105, and for connecting BV with EC. This work was supported by a Berkeley Excellence Account for Research and the NSF. Matija Čuk alerted us to the misprint in Y03 and provided insights that were most helpful. We thank Smadar Naoz for an encouraging and constructive referee's report; Konstantin Batygin, Alexandre Correia, Bekki Dawson, Eve Lee, Yoram Lithwick, and Renu Malhotra for useful discussions and feedback; and Daniel Tamayo for teaching us how to use REBOUND.

## REFERENCES

- Bailey M. E., Chambers J. E., Hahn G., 1992, *Astronomy and Astrophysics*, 257, 315
- Batygin K., Morbidelli A., 2017, preprint, ([arXiv:1710.01804](https://arxiv.org/abs/1710.01804))
- Carruba V., 2002, *Icarus*, 158, 434
- Dawson R. I., Chiang E., 2014, *Science*, 346, 212
- Farago F., Laskar J., 2010, *MNRAS*, 401, 1189
- Gallardo T., Hugo G., Pais P., 2012, *Icarus*, 220, 392
- Katz B., Dong S., Malhotra R., 2011, *Physical Review Letters*, 107, 181101
- Kozai Y., 1962, *The Astronomical Journal*, 67, 591
- Kushnir D., Katz B., Dong S., Livne E., Fernández R., 2013, *The Astrophysical Journal*, 778, L37
- Lee E. J., Chiang E., 2016, *The Astrophysical Journal*, 827, 125
- Lidov M. L., 1962, *Planetary and Space Science*, 9, 719
- Lithwick Y., Naoz S., 2011, *The Astrophysical Journal*, 742, 94
- Macintosh B., et al., 2015, *Science*, 350, 64
- Murray C. D., Dermott S. F., 2000, *Solar System Dynamics*. "Cambridge University Press"
- Naoz S., 2016, *ARA&A*, 54, 441
- Naoz S., Farr W. M., Lithwick Y., Rasio F. A., Teyssandier J., 2011, *Nature*, 473, 187
- Naoz S., Li G., Zanardi M., de Elía G. C., Di Sisto R. P., 2017, *The Astronomical Journal*, 154, 18
- Nesvold E. R., Naoz S., Vican L., Farr W. M., 2016, *The Astrophysical Journal*, 826, 19
- Nesvorny D., Alvarellos J. L. A., Dones L., Levison H. F., 2003, *The Astronomical Journal*, 126, 398
- Pearce T. D., Wyatt M. C., 2014, *Monthly Notices of the Royal Astronomical Society*, 443, 2541
- Rein H., Liu S.-F., 2012, *A&A*, 537, A128
- Rein H., Tamayo D., 2015, *MNRAS*, 452, 376
- Sheppard S. S., Trujillo C., 2016, *The Astronomical Journal*, 152, 221
- Silsbee K., Tremaine S., 2016, *The Astronomical Journal*, 152, 103
- Silsbee K., Tremaine S., 2017, *The Astrophysical Journal*, 836, 39
- Thomas F., Morbidelli A., 1996, *Celestial Mechanics*, 64, 209

**Table A1.** Initial conditions for Figure 3 ( $R = -0.05032$ ).

$e_2$	$\Omega_2$ (rad)	$\varpi_2$ (rad)	$I$ (rad)	$J_{z,\text{init}}$
Center Panel ( $e_1 = 0.1$ , $\varpi_1 = 0$ )				
0.2110	0	1.5708	1.1170	0.4285
0.2110	0	1.5708	2.0246	-0.4285
0.4165	0	1.5708	1.0821	0.4268
0.4165	0	1.5708	2.0595	-0.4268
0.6738	0	0	1.0123	0.3916
0.6738	0	0	2.1293	-0.3916
Bottom Panel ( $e_1 = 0.3$ , $\varpi_1 = 0$ )				
0.1094	0	1.5708	1.4486	0.1212
0.1094	0	1.5708	1.6930	-0.1212
0.5575	0	0	1.3264	0.2009
0.5575	0	0	1.8151	-0.2009
0.7061	0	0	1.3264	0.1713
0.7061	0	0	1.8151	-0.1713

- Tremaine S., Yavetz T. D., 2014, *American Journal of Physics*, 82, 769
- Verrier P. E., Evans N. W., 2008, *MNRAS*, 390, 1377
- Verrier P. E., Evans N. W., 2009, *MNRAS*, 394, 1721
- Wisdom J., Holman M., 1991, *AJ*, 102, 1528
- Wu Y., Murray N., 2003, *The Astrophysical Journal*, 589, 605
- Wyatt M. C., Dermott S. F., Telesco C. M., Fisher R. S., Grogan K., Holmes E. K., Piña R. K., 1999, *The Astrophysical Journal*, 527, 918
- Yokoyama T., Santos M. T., Cardin G., Winter O. C., 2003, *Astronomy and Astrophysics*, 401, 763
- Zanardi M., de Elía G. C., Di Sisto R. P., Naoz S., Li G., Guilera O. M., Brunini A., 2017, *Astronomy and Astrophysics*, 605, A64

## APPENDIX A: INITIAL CONDITIONS

This paper has been typeset from a  $\text{\TeX}/\text{\LaTeX}$  file prepared by the author.

**Table A2.** Initial conditions for Figure 12 ( $e_1 = 0.1$ ,  $\varpi_1 = 0$ ).

color	$e_2$	$\Omega_2$ (rad)	$\varpi_2$ (rad)	$I$ (rad)
$R = 0.3000$				
black	0.3189	0.0000	0.0000	0.0175
violet	0.3974	0.0000	0.0000	0.2443
red	0.5421	0.0000	0.0000	0.0454
dark blue	0.4656	-0.7854	0.0000	0.3491
turquoise	0.6604	-0.7854	0.0000	0.5934
$R = 0.0721$				
black	0.0678	-0.7854	0.0000	0.7592
violet	0.1894	-0.7854	0.0000	0.7679
red	0.3685	-0.7854	0.0000	0.7941
dark blue	0.4556	-0.7854	0.0000	0.8116
turquoise	0.6036	0.0000	0.0000	0.8465
blue	0.0957	-1.5708	0.0000	0.7505
gray	0.6683	-1.5708	0.0000	0.8552
$R = -0.0721$				
black	0.0072	-1.5708	0.0000	1.1519
violet	0.5842	0.0000	0.0000	1.0821
red	0.2535	0.0000	0.3491	1.1868
dark blue	0.4882	0.0000	0.9076	1.1170
turquoise	0.4882	-3.1416	0.9076	1.1170
blue	0.3832	0.0000	1.3963	1.1519
gray	0.1479	0.0000	1.4661	1.2042
yellow	0.2485	0.0000	1.5359	1.1868
$R = -0.0938$				
black	0.0787	0.0000	0.0000	1.3177
violet	0.1563	-0.7854	0.0000	1.2654
red	0.2028	-0.7854	0.0000	1.2566
dark blue	0.2733	-0.7854	0.0000	1.2392
turquoise	0.5353	0.0000	0.1396	1.1519
blue	0.3088	0.0000	0.4189	1.2566
gray	0.5957	0.0000	0.6981	1.1170
yellow	0.4617	0.0000	1.3963	1.1868
$R = -0.1373$				
black	0.3691	0.0000	0.0000	1.4835
violet	0.3500	0.0000	0.3491	1.5533
red	0.4684	0.0000	0.6283	1.3439
dark blue	0.3565	0.0000	0.8378	1.5185
turquoise	0.3326	0.0000	0.2793	1.0996
blue	0.5176	0.0000	1.2566	1.2915

**Table A3.** Initial conditions for Figure 13 ( $e_1 = 0.3$ ,  $\varpi_1 = 0$ ).

color	$e_2$	$\Omega_2$ (rad)	$\varpi_2$ (rad)	$I$ (rad)
$R = 0.3000$				
black	0.3207	0.0000	0.0000	0.2443
violet	0.4371	0.0000	0.0000	0.4014
red	0.5534	-1.5708	0.0000	0.4712
dark blue	0.6588	-1.5708	0.0000	0.6283
turquoise	0.2110	-1.5708	0.0000	0.0175
$R = 0.0503$				
black	0.3279	0.0000	0.0000	0.9948
violet	0.4362	0.0000	0.0000	1.0123
red	0.6553	0.0000	0.0000	1.0821
dark blue	0.5130	0.0000	0.0000	1.0297
turquoise	0.0817	-0.7854	0.0000	0.8378
blue	0.2608	-0.7854	0.0000	0.8552
$R = 0.0000$				
black	0.2127	-0.7854	0.0000	0.9687
violet	0.3300	-0.7854	0.0000	0.9774
red	0.4942	-0.7854	0.0000	0.9948
dark blue	0.0985	-1.5708	0.0000	0.8465
turquoise	0.5784	-1.5708	0.0000	0.9163
$R = -0.0503$				
black	0.3380	-0.7854	0.0000	1.0996
violet	0.3380	-3.9270	0.0000	1.0996
red	0.2444	0.0000	0.0000	1.4224
dark blue	0.0667	0.0000	0.0000	1.4573
turquoise	0.3295	0.0000	0.0000	1.3963
blue	0.4364	0.0000	0.0000	1.3614
gray	0.5576	0.0000	0.0000	1.3265
yellow	0.7061	0.0000	0.0000	1.3265
$R = -0.0721$				
black	0.4081	-0.7854	0.0000	1.1519
violet	0.4937	0.0000	0.0000	1.5184
red	0.5541	0.0000	0.0000	1.4486

**Table A4.** Initial conditions for Figure 14 ( $e_1 = 0.7$ ,  $\varpi_1 = 0$ ).

color	$e_2$	$\Omega_2$ (rad)	$\varpi_2$ (rad)	$I$ (rad)
$R = 0.5500$				
black	0.4587	0.0000	0.0000	0.0175
violet	0.4629	0.0000	0.0000	0.1309
red	0.4629	0.0000	0.0000	0.2443
dark blue	0.4670	0.0000	0.0000	0.3316
turquoise	0.4716	0.0000	0.0000	0.4014
blue	0.4887	0.0000	0.0000	0.5760
gray	0.5211	0.0000	0.0000	0.7941
$R = 0.5000$				
black	0.3783	0.0000	0.0000	0.0175
violet	0.4053	0.0000	0.0000	0.4014
red	0.4607	0.0000	0.0000	0.7156
dark blue	0.5016	0.0000	0.0000	0.8988
$R = 0.4000$				
black	0.4413	-1.5708	0.0000	0.3403
violet	0.3368	-1.5708	0.0000	0.2705
red	0.2432	-0.7854	0.0000	0.3054
dark blue	0.0023	0.0000	0.0000	0.6458
turquoise	0.1348	0.0000	0.0000	0.6021
blue	0.2600	0.0000	0.0000	0.7069
$R = 0.3000$				
black	0.0096	0.0000	0.0000	1.1606
violet	0.0267	0.0000	0.0000	1.1519
red	0.0051	-1.5708	0.0000	0.3665
dark blue	0.2154	-0.7854	0.0000	0.5149
turquoise	0.3407	-0.7854	0.0000	0.5672
$R = 0.2650$				
black	0.0088	0.0000	0.0000	1.4399
violet	0.0239	0.0000	0.0000	1.4224
red	0.1103	0.0000	0.0000	1.3875
dark blue	0.2154	0.0000	0.0000	1.4748
turquoise	0.2098	-0.7854	0.0000	0.5760

**Table A5.** Initial conditions for Figure 15 ( $\varpi_1 = 0$ ).

$e_1$	$e_2$	$\Omega_2$ (rad)	$\varpi_2$ (rad)	$I$ (rad)
Panel (a) $\omega_2$ resonance				
0.1	0.3000	-1.5708	0.0000	1.0917
Panel (b) $\Omega_2 - \varpi_1$ resonance				
0.7	0.5250	2.3562	2.3562	1.0137
Panel (c) $\varpi_2 - \varpi_1$ resonance				
0.7	0.2000	0.0000	0.0000	0.6500
Panel (d) $\varpi_2 + \varpi_1 - 2\Omega_2$ resonance				
0.1	0.0787	0.0000	0.0000	1.3177
Panel (e) $\varpi_2 - 3\varpi_1 + 2\Omega_2$ resonance				
0.7	0.7000	0.0000	0.0000	1.3000